ACS APPLIED MATERIALS & INTERFACES

Research Article

www.acsami.org

Component-Controlled Synthesis and Assembly of Cu–Pd Nanocrystals on Graphene for Oxygen Reduction Reaction

Yulin Zheng,[†] Shulin Zhao,[†] Suli Liu,[†] Huanhuan Yin,[†] Yu-Yun Chen,[†] Jianchun Bao,[†] Min Han,*[,†,‡] and Zhihui Dai*[,†]

[†]Jiangsu Key Laboratory of Biofunctional Materials, School of Chemistry and Materials Science, Nanjing Normal University, Nanjing 210023, People's Republic of China

[‡]State Key Laboratory of Coordination Chemistry, Nanjing National Laboratory of Solid State Microstructures, Nanjing University, Nanjing 210093, People's Republic of China

Supporting Information

ABSTRACT: Exploring low-cost, high-activity, and long-durability hybrid electrocatalysts for cathodic oxygen reduction reaction (ORR) is vital to advance fuel cells technologies. In this paper, a series of graphene (G)–Cu_xPd_y (Cu_4Pd, Cu_3Pd, CuPd, $CuPd_3$, $CuPd_4$) nanocomposites (G–Cu_xPd_y NCPs) is obtained by assembly of Cu_xPd_y alloy nanocrystals (NCs) with controlled component ratios on G nanosheets using the "dispersing–mixing–vaporizing solvent" strategy and used as electrocatalysts for ORR. Compared with pure Cu_xPd_y NCs, greatly enhanced interfacial electron transfer dynamics are observed in G–Cu_xPd_y NCPs, which show a strong correlation with the alloy compositions of the NCPs. The electrocatalytic experiments in alkaline solution reveal that the ORR activities of those G–Cu_xPd_y NCPs are also strongly dependent on alloy components and exhibit a double-volcano feature with variations of alloy components. Among them, G–Cu_3Pd NCPs possess the highest electrocatalytic activity, which is much better than some reported electrocatalysts and commercial Pd/C catalyst and close to Pt/C catalyst. By correlating the Pd 3d binding energies and the sizes of Cu_xPd_y NCs with the mass-specific activities of G–Cu_xPd_y NCPs and considering the interfacial electron transfer dynamics, the best catalytic activity of G–Cu_3Pd NCPs may result from the unique electronic structure and the smallest size of Cu_3Pd NCs as well as the strong synergistic effect between G and Cu_3Pd NCs. Moreover, the durability of G–Cu_3Pd NCPs is superior to that of Pt/C catalyst, indicating that they are promising cathodic electrocatalysts for using in alkaline fuel cells.

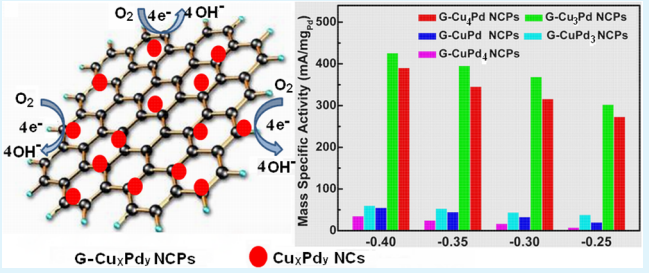

KEYWORDS: *nanocomposites, graphene, bimetallic nanocrystals, assembly, electrocatalysis, oxygen reduction reaction*

1. INTRODUCTION

As a monolayer of sp^2-hybridized carbon atoms with hexagonal honeycomb-like structure, graphene (G) possesses a very high theoretical surface area (~2630 m^2 g^{-1}), high electrical conductivity, excellent mechanical and thermal conductivity, and proton transport performance, which has potential applications in electronics, energy storage, sensing, separation, and catalysis fields.[1−6] For catalytic application, it is usually used as a support to stabilize or transfer photogenerated electrons or enhance conductivity of special photocatalysts or electrocatalysts.[7,8] To improve the performance of desired catalysts, the key lies on efficiently integrating active components on G and enhancing their interaction or coupling.[9] For perfect G, only weak physical interaction (e.g., $\pi-\pi$ stacking) can be utilized, which is not an ideal choice for integrating catalyst particles, while the G obtained by chemical oxidation exfoliation of natural graphite and then reduction strategy has a large amount of defects and residual organic functional groups,[10] which can provide the "landing" sites for specific catalyst particles. Thus, it is usually chosen as raw material for fabricating G-based hybrid catalysts. This has been demonstrated in the Pt or Pd-based nanocrystals (NCs) catalysts grown on G for electrocatalytic reactions,[11,12] in the promotion of semiconducting NCs (e.g. $Zn_xCd_{1-x}S$) by G for solar photocatalytic H_2 production,[13] and in the activation of Co_3O_4 and CoS_x NCs as well as cobalt porphyrin multilayers by G for oxygen reduction reaction (ORR) in alkaline media.[14−16] In those works, the NCs catalysts were directly grown on G surface to maximize G–NCs contact and to achieve desired enhancement of the catalysts. However, using the in situ growth method, the size, shape, and component of the NCs are difficult to be controlled, and thereby their catalytic potentials may not be fully realized. In view of recent great progress in the solution-phase synthesis of monodisperse NCs, assembly of presynthesized monodisperse NCs on G to form well-coupled G–NCs nanocomposites (NCPs) may be a better avenue for

Received: December 12, 2014
Accepted: February 19, 2015
Published: February 19, 2015

DOI: 10.1021/acsami.5b01541
ACS Appl. Mater. Interfaces 2015, 7, 5347−5357

optimizing the catalytic performance of desired NCs. For instance, by organizing the presynthesized small-sized monodisperse Fe−Pt NCs on G, the well-coupled G/Fe−Pt NCs NCPs have been obtained in Sun's group.[17] Compared with pure Fe−Pt NCs as well as conventional carbon material supported Fe−Pt NCs catalyst, those NCPs exhibit greatly enhanced electrocatalytic activity and stability for ORR. This work demonstrates that G is actually a better supporter for organizing the active NCs and promoting their application in catalytic fields.

Recently, Cu and Cu-based alloy NCs have attracted much attention because they possess good electronic conductivity and excellent mechanical and catalytic properties and have potential applications in electronics, flexible electrode, mechanical engineering, fine chemicals, and energy storage and conversion devices.[18−21] The excellent electrocatalytic performance along with high abundance in earth has made Cu gradually become a rising star in clean energy fields. For instance, the oxide-derived nanocrystalline Cu[22] and Cu nanofoams[23] are found to be highly efficient electrocatalysts for reduction of CO and CO_2 to produce clean fuels, respectively. In addition, the ultrathin Cu nanobelts prepared by a colloidal self-assembly strategy[24] and the bioinspired Cu catalyst[25] are identified to possess high electrocatalytic activity toward ORR in alkaline media. To further improve the performance of those Cu catalysts, alloying them with some noble metals (e.g., Pt, Au) to obtain special alloy NCs with well-controlled size, component, and geometrical structures may be one of the feasible avenues. For example, Cu_3Pt hollow nanostructures show much higher electrocatalytic activity than commercial Pt/C for ORR in acidic media.[26] Also, CuAu intermetallic NCs directly grown on Vulcan XC-72 C can efficiently electrocatalyze ORR in alkaline media.[27] In contrast to Cu−Pt and Cu−Au alloy systems, Cu−Pd alloy has two obvious advantages: (1) its cost is lower than that of Cu−Pt and Cu−Au alloys because Pd is relatively cheaper than Pt and Au; (2) the lattice mismatch degree and the difference of atomic radius between Cu and Pd are much lower than that of Cu and Pt or Au, beneficial to form alloy in a wide component range. To date, several Cu−Pd alloy nanostructures, such as spherical NCs,[28−33] nanocubes and irregular polyhedral as well as tetrapod-like NCs,[34] core/shell heterostructure,[35] hollow nanospheres,[36] nanorods,[37] nanotubes,[38] and tubular mesoporous or porous structures,[39,40] have been fabricated via different synthetic strategies. Although great progress has been achieved in Cu−Pd alloy NCs fields, there are still some limitations that need to be improved: (1) To the best of our knowledge, the ordered alloy phase structure has not been achieved using solution-phase synthetic route; (2) The Cu−Pd NCs with well-controlled shapes have been obtained, but their sizes are usually larger than 10 nm; (3) The componential ratio of special alloy NCs has a great impact on electronic coupling that determines their catalytic performance.[41,42] Though some works involve the componential ratio control of Cu−Pd NCs, the componential ratios of currently obtained Cu−Pd NCs are still very limited, and their correlation with catalytic performance is not systematically studied. Besides these challenges on synthesis, the current applications of Cu−Pd alloy NCs are focused on catalytic oxidation of alcohols or formic acid, synthesis of ammonia, and electrocatalytic ORR. As for ORR, most works are concentrated on acidic media and a report in alkaline media is rare. In view of those limitations, component-controlled synthesis of small-sized Cu−Pd NCs and study of their ORR performances in alkaline media has become an interesting topic.

In this paper, small-sized Cu_xPd_y NCs including Cu_4Pd, Cu_3Pd, CuPd, $CuPd_3$, and $CuPd_4$ are first synthesized and then assembled on G sheets to obtain a series of G−Cu_xPd_y NCPs, which are used as electrocatalysts for ORR in alkaline media. The typical synthesis of Cu_xPd_y NCs is based on thermal decomposition of $Pd(acac)_2$ and $Cu(acac)_2$ in the liquid mixture of oleylamine and triethylene glycol. By simply adjusting the molar ratio of metallic precursors, the componential ratios of Cu and Pd in finally obtained Cu_xPd_y NCs can be well controlled. Using a facile "dispersing−mixing−vaporizing solvent" strategy, nearly monodisperse Cu_xPd_y NCs can be integrated on the planar planes, crumples, or edges of G sheets to generate desired G−Cu_xPd_y NCPs. Besides the composition and microstructure of those G−Cu_xPd_y NCPs, their interfacial electron transfer dynamics are also investigated by electrochemical impedance spectra, which are greatly improved in contrast to pure Cu_xPd_y NCs and show a strong correlation with the alloy components of the NCPs. Among them, the G−Cu_3Pd NCPs exhibit the fastest interfacial electron transfer dynamics, so they are taken as an emphasis to study electrocatalytic ORR performances. The related ORR mechanism is suggested based on the electrocatalytic dynamic experiments. In addition, under identical conditions, the electrocatalytic performance of G−Cu_3Pd NCPs is also compared with other G−Cu_xPd_y NCPs and some reported electrocatalysts as well as commercial Pd/C and Pt/C catalysts. The results reveal that G−Cu_3Pd NCPs are the best electrocatalysts among those G−Cu_xPd_y NCPs, showing great promise as an alternative electrocatalyst for Pt/C to apply in alkaline fuel cells. Moreover, the possible origin of the best electrocatalytic performance of G−Cu_3Pd NCPs is also discussed.

2. EXPERIMENTAL SECTION

2.1. Synthesis of Cu_xPd_y NCs. To describe simply, we take the Cu_3Pd NCs as an example to introduce the synthetic process. In a typical synthesis, 0.1 mmol of $Pd(acac)_2$, 0.3 mmol of $Cu(acac)_2$, 5 mL of oleylamine (OLA), and 4 mL of triethylene glycol were added into a clean three-necked flask in turn. Also, a blue suspension was formed by treating the above mixture in an ultrasonic bath for 2 min at room temperature. After degassing for 30 min, the reactor was heated from room temperature to 240 °C at a rate of 3 °C min^{-1} under Ar atmosphere and kept at 240 °C for 40 min. During this process, the color of the reaction system changed from blue to deep green and finally turned to dark brown. After naturally cooling down to room temperature, the black solid was separated by centrifugation and washed with *n*-heptane and absolute ethanol to remove byproducts. Finally, the product was dried in vacuum at 40 °C for 2 h and used for analysis and characterization.

The synthesis and post-treatment procedures of other Cu_xPd_y NCs were similar to that for Cu_3Pd NCs. Keeping other reaction conditions constant and only changing the mole ratios of used metal precursors, the Cu_4Pd, CuPd, $CuPd_3$, and $CuPd_4$ NCs were also obtained.

2.2. Synthesis of Graphene (G) Nanosheets. In a typical synthesis, 20 mg of presynthesized GO nanosheets according to a modified Hummers' method[43] was dispersed in 50 mL of dimethylformamide (DMF) by treating in an ultrasonic bath for 30 min. Then, this solution was transferred to a clean three-necked flask and refluxed at 160 °C for 1 h. Finally, the reactor was naturally cooled down to room temperature. After being separated and washed with deionized water several times, the product was dried in vacuum at 40 °C for 2 h and used for further characterization.

2.3. Assembly of Cu_xPd_y NCs on G To Form G−Cu_xPd_y NCPs. First, 10 mg of presynthesized G nanosheets and 15 mg of Cu_xPd_y

DOI: 10.1021/acsami.5b01541
ACS Appl. Mater. Interfaces 2015, 7, 5347−5357

NCs were dispersed in 10 mL of DMF and 10 mL of *n*-hexane by treating in an ultrasonic bath to form a homogeneous suspension, respectively. Subsequently, the two suspensions were mixed in a flask under vigorous magnetic stirring for 1 h. Finally, the reactor was heated to 95 °C under reduced pressure to vaporize the solvent and then allowed to cool down to room temperature. After being washed with dilute acetic acid and absolute ethanol 3 times, the product was dried in vacuum at 40 °C for 2 h and used for further characterization.

2.4. Material Characterization. The transmission electron microscopy (TEM) images were taken on a JEM-200CX instrument (Japan) with an accelerating voltage of 200 kV. High-resolution (HRTEM) images were carried out on a JEOL-2100F apparatus at an accelerating voltage of 200 kV. The X-ray energy-dispersive spectra (EDS) were taken on a JSM-5610LV-Vantage-typed energy spectrometer. The X-ray diffraction (XRD) patterns were acquired on a D/max 2500VL/PC diffractometer equipped with graphite-monochromatized Cu Kα radiation (λ = 1.54060 A) in 2θ ranging from 10° to 90°. Corresponding work voltage and current were 40 kV and 100 mA, respectively. Induction couple plasma (ICP) measurements were performed on a Jarrel-Ash 1100 + 2000 Quantometer. X-ray photoelectron spectra (XPS) were obtained on a scanning X-ray microprobe (PHI 5000 Verasa, ULAC-PHI, Inc.) using Al Kα radiation. Binding energies were calibrated using the C 1s peak (BE = 284.6 eV) as standard. The electrochemical impedance spectra (EIS) tests were carried out on a PGSTAT30/FRA2 system (Autolab, Netherlands) in 10 mM potassium ferricyanide containing 0.1 M KCl. The EIS were recorded within the frequency range of 10^{-2}–10^{6} Hz. The amplitude of the applied sine wave potential in each case was 5 mV.

2.5. Electrocatalytic Measurements. The electrocatalytic experiments were carried out on a Gamry's Rotating Electrode (RDE 700e) with a glassy carbon disk (5 mm in diameter). A standard three-electrode system was used for all tests. The platinum sheet and saturated calomel electrode (SCE) were used as the counter electrode and reference electrode, respectively. The G–Cu_xPd_y NCPs modified glassy carbon disk electrodes (GCEs) were used as the working electrode, which were fabricated according to the following procedure: 4 mg of G–Cu_xPd_y NCPs was dispersed in 2 mL of ethanol and water (with a volume ratio of 1:3) to form a homogeneous catalyst ink. A 10 μL amount of such catalyst ink was coated on pretreated GCEs by a microliter syringe. After drying in a gentle N_2 stream, 5 μL of 1% Nafion solution was dropped onto the electrode surface. Thus, the G–Cu_xPd_y NCPs modified GCEs were fabricated. For comparison, the commercial 10% Pd/C (purchased from Alfa Asea) and 20% Pt/C (purchased from Alfa Asea) catalysts modified GCEs were also prepared using the same procedure. O_2 reduction reactions were examined by first bubbling the electrolyte solution (0.1 M KOH) with high-purity O_2 for 20 min and then blanketing the solution with an O_2 atmosphere during the entire experiment. All potentials in this study were reported with respect to SCE, and all experiments were performed at room temperature.

3. RESULTS AND DISCUSSION

The compositions of the obtained Cu_4Pd, Cu_3Pd, CuPd, $CuPd_3$, and $CuPd_4$ NCs were first identified by EDS and ICP. The corresponding data are summarized in Table S1, Supporting Information. The EDS results are consistent with ICP analysis, confirming that the molar ratios of Cu and Pd in finally obtained Cu_xPd_y NCs are very close to that of initial metal precursors. Further evidence comes from XRD analysis (Figure S1, Supporting Information). In the 20° < 2θ < 90° range, four obvious diffraction peaks can be observed for those Cu_xPd_y NCs, indicating that they are well crystallized. The positions of their diffraction peaks are located between that of face-centered cubic phase (fcc) Cu and fcc Pd, indicating that they are Cu–Pd alloy NCs and their phase structures are still fcc. Additionally, with the increase of Cu atomic or molar percentage, the diffraction peaks of obtained Cu_xPd_y NCs will shift to high angle direction, which are very close to that of pure Cu. While increasing the Pd molar percentage, the diffraction peaks of generated Cu_xPd_y NCs gradually shift to the low-angle direction, which are close to that of pure Pd. According to Vegard's law, the Cu and Pd atomic ratios in those Cu_xPd_y NCs are further calculated, which are in accordance with EDS and ICP analysis. The shapes and microstructures of those Cu_xPd_y NCs were further examined by TEM and HRTEM. Figure 1A

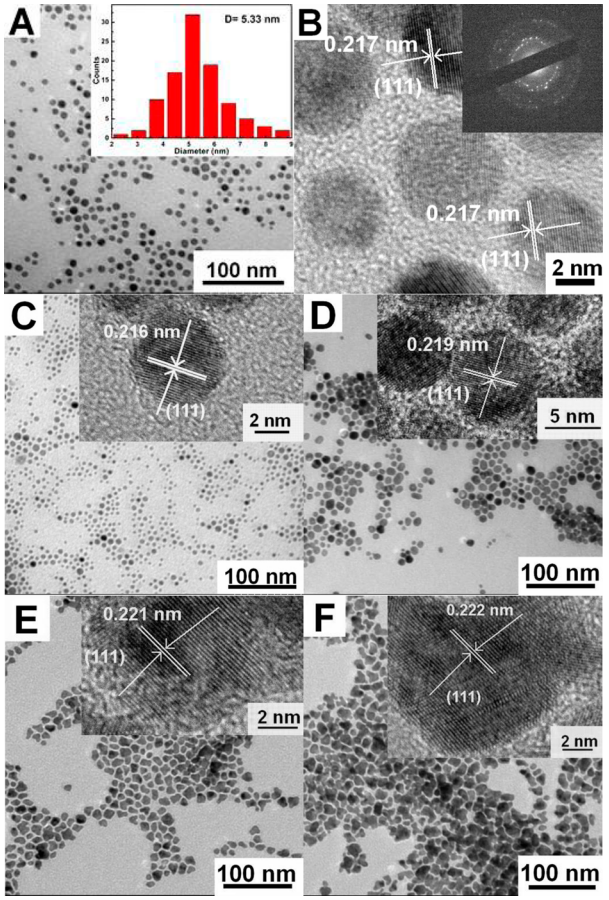

Figure 1. (A) TEM image of as-synthesized Cu_3Pd NCs. (Inset) Corresponding size statistical distribution picture. (B) HRTEM image of the Cu_3Pd NCs. (Inset) Related SAED pattern. (C–F) TEM images of the obtained Cu_4Pd (C), CuPd (D), $CuPd_3$ (E), and $CuPd_4$ (F) NCs. (Insets) Their corresponding HRTEM images.

shows the TEM image of the Cu_3Pd NCs synthesized under the typical condition, from which large-area monodisperse NCs with the quasi-spherical shape can be observed. The statistical analysis (inset of Figure 1A) reveals that their average size is about 5.3 nm. The corresponding HRTEM image (Figure 1B) exhibits clear lattice fringes, and the lattice spacing is about 2.17 Å, corresponding to the interplanar separation of the (111) plane of fcc Cu_3Pd. The selected area electron diffraction pattern (inset of Figure 1B) shows the obvious spots and rings, further proving that they are well crystallized. Similarly, other Cu_xPd_y NCs, such as Cu_4Pd, CuPd, $CuPd_3$, and $CuPd_4$, are also characterized by TEM and HRTEM, shown in Figure 1C–F. These four kinds of Cu_xPd_y NCs are also nearly monodisperse and well crystallized. Additionally, their morphologies are found to change with the Cu and Pd molar ratio. With the increase of Cu molar ratio, the shape of the obtained alloy NCs gradually turns into quasi-spherical that close to pure Cu NCs (Figure

DOI: 10.1021/acsami.5b01541
ACS Appl. Mater. Interfaces 2015, 7, 5347–5357

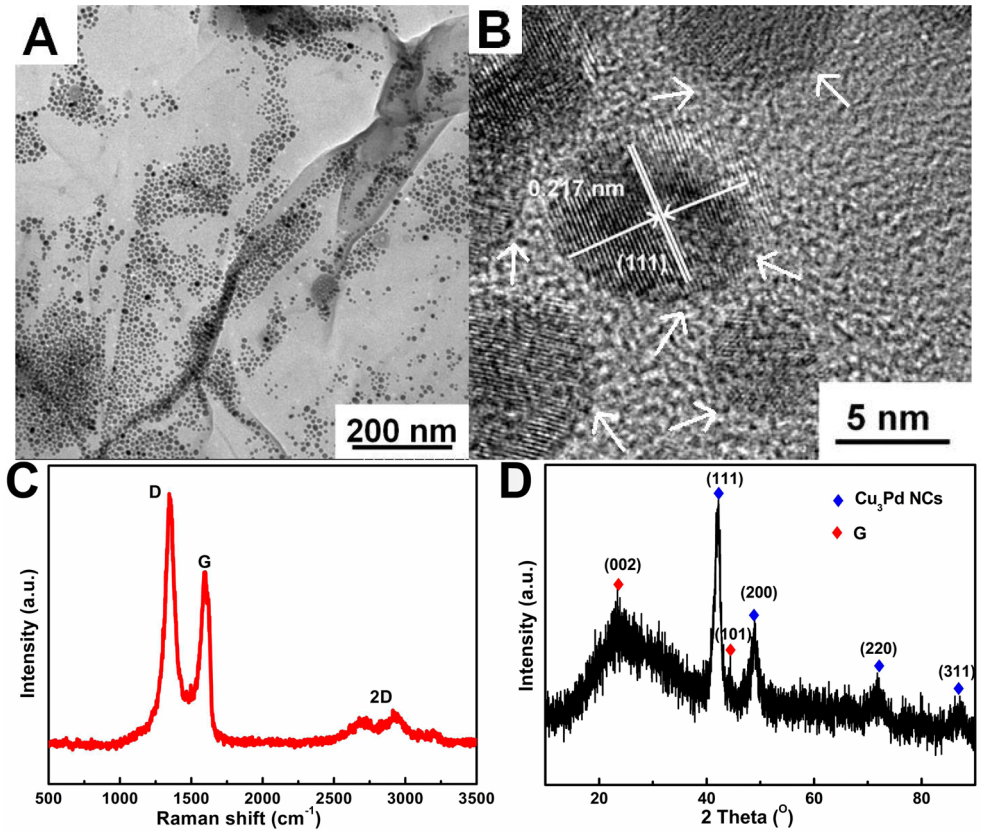

Figure 2. (A) TEM image of the as-synthesized G−Cu_3Pd NCPs. (B) Corresponding HRTEM image of the G−Cu_3Pd NCPs. (C) Raman spectrum and (D) XRD pattern of the G−Cu_3Pd NCPs.

S2A, Supporting Information). While increasing the Pd molar ratio, the shape of the obtained alloy NCs tends to branch-like, just like that of pure Pd NCs (Figure S2B, Supporting Information). Moreover, it is reported that the componential ratio of alloy NCs has a great impact on their surface electronic structures and catalytic properties. To study the surface structures and electronic coupling effect, the XPS tests for Cu_4Pd, Cu_3Pd, CuPd, $CuPd_3$, and $CuPd_4$ NCs are also performed, shown in Figure S3, Supporting Information. A detailed discussion is given in Figure S3, Supporting Information. The results demonstrate that the Cu_3Pd NCs may be chemically ordered alloy phase and possess a unique surface electronic structure compared with that of Cu_4Pd, CuPd, $CuPd_3$, and $CuPd_4$ NCs.

By assembling those Cu_xPd_y NCs on G nanosheets, the desired G−Cu_xPd_y NCPs can be obtained. Figure 2A shows the typical TEM image of the as-synthesized G−Cu_3Pd NCPs, from which we can see many small-sized black dots anchored on the planar planes, crumples, or edges of light-colored thin sheets. In contrast to pure G (Figure S4, Supporting Information), the observed black dots can be assigned to the assembled Cu_3Pd NCs and the light-colored thin sheets are the G. From the HRTEM image (Figure 2B), the interfaces between the Cu_3Pd NC and G can be clearly observed (see the white arrows marked regions). Besides the interfaces, the clear lattice fringes are observed for an individual Cu_3Pd NC and the lattice spacing is about 2.17 Å, corresponding to the interplanar separation of the (111) plane of fcc Cu_3Pd. To identify the microstructure of the G component in the NCPs, the Raman spectrum is further performed because it is a powerful tool for detecting ordered (sp^2 C, G band) and disordered (sp^3 C, D band) crystalline structure as well as the layer number of G.[44] Figure 2C gives the Raman spectrum of the G−Cu_3Pd NCPs. Two characteristic Raman peaks observed at about 1347 and 1595 cm^{-1} are assigned to D and G bands of the G component, respectively. Additionally, a small broad peak can be seen at about 2500−3000 cm^{-1} that corresponds to the 2D band of G, implying that the G component in the NCPs is a few layers, not a single layer.[45] Moreover, compared with pure G, the D and G bands of G in the NCPs are red shifted about 2 cm^{-1} (Figure S5, Supporting Information), suggesting that there is a strong coupling of G and Cu_3Pd in obtained NCPs.[46] Furthermore, the composition of the G−Cu_3Pd NCPs is further examined by XRD, shown in Figure 2D. In the 2θ ranging from 10° to 90°, four obvious and sharp diffraction peaks along with a very broad peak as well as a small peak are observed. The four diffraction peaks at about 42.4°, 49.1°, 72.7°, and 87.3° marked with blue rhombuses can be indexed to the (111), (200), (220), and (311) planes of cubic-phase Cu_3Pd. Excluding them, the broad peak centered at 25.7° and the small peak at about 43.1° labeled with red rhombuses are assigned to the characteristic (002) and (101) planes of hexagonal graphite structure (JCPDS-65-6212) that originate from G. On the basis of the above analysis, we can confirm that the Cu_3Pd NCs have been successfully integrated on G to form well-coupled NCPs.

In addition, besides G−Cu_3Pd NCPs, other G−Cu_xPd_y NCPs including G−Cu_4Pd, G−CuPd, G−$CuPd_3$, and G−$CuPd_4$ are also fabricated using the similar synthetic strategy. Figure 3 provides the corresponding TEM images for those four kinds of NCPs. In each of those NCPs, the related Cu_xPd_y alloy NCs are well dispersed on the surfaces of G nanosheets, which provides multiple additional interfaces and facilitates

DOI: 10.1021/acsami.5b01541
ACS Appl. Mater. Interfaces 2015, 7, 5347−5357

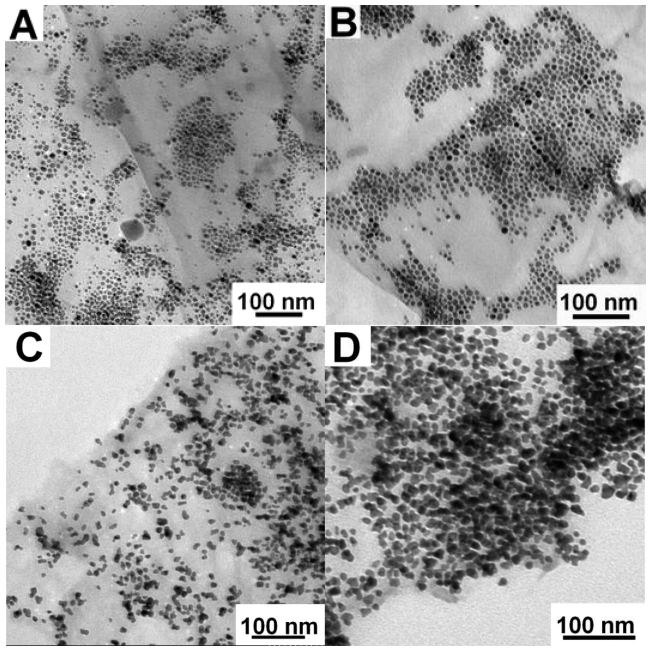

Figure 3. TEM images for (A) G−Cu_4Pd, (B) G−CuPd, (C) G−$CuPd_3$, and (D) G−$CuPd_4$ NCPs.

catalytic application. The compositions of those NCPs are further identified by EDS and XRD, shown in Figures S6 and S7, Supporting Information, respectively. The results confirm that those NCPs are composed of G and Cu_xPd_y (Cu_4Pd, CuPd, $CuPd_3$, and $CuPd_4$) NCs.

As a powerful and sensitive technique, the electrochemical impedance spectrum (EIS) provides information about the interfacial properties of the surface-modified electrode. To study the interfacial electron transfer dynamics of those five kinds of G−Cu_xPd_y NCPs, they are modified on glassy carbon electrodes (GCEs) and used for EIS tests. Figure 4A and 4B shows the typical EIS spectra (Nyquist curves) for various G−Cu_xPd_y NCPs modified GCEs. For comparison, the Nyquist curves for pure Cu_xPd_y NCs modified GCEs are also measured and given in Figure S8, Supporting Information. Except for the semicircles observed at the high-frequency to midfrequency region, the linear tails are observed from the Nyquist curves of G−Cu_xPd_y NCPs and pure Cu_xPd_y NCs at the low-frequency region, indicating that the concentration polarization cannot be ignored. The intersection angles of the linear tails with the real axis (represented by Z′ in Figure 4 and Figure S8, Supporting Information) are close to 45°, implying the presence of the ideal Warburg diffusion impedance. Additionally, the first intersection point with the real axis at the high-frequency region is not zero, indicating the series of internal resistance also cannot be ignored. Thus, the electrochemical processes observed from the Nyquist curves of G−Cu_xPd_y NCPs and pure Cu_xPd_y NCs modified GCEs are represented by the modified Randles equivalent circuits with a set of resistors and constant phase elements (CPE) in series and parallel, as shown in Figures S9 and S10, Supporting Information. There are four components in each equivalent circuit, which are labeled as R_s, R_{et}, W, and CPE. The detailed physical meanings of those four components are as follows: (1) R_s represents the resistance of the electrolyte and intrinsic resistance of active materials modified on electrode; (2) R_{et} stands for electron or charge

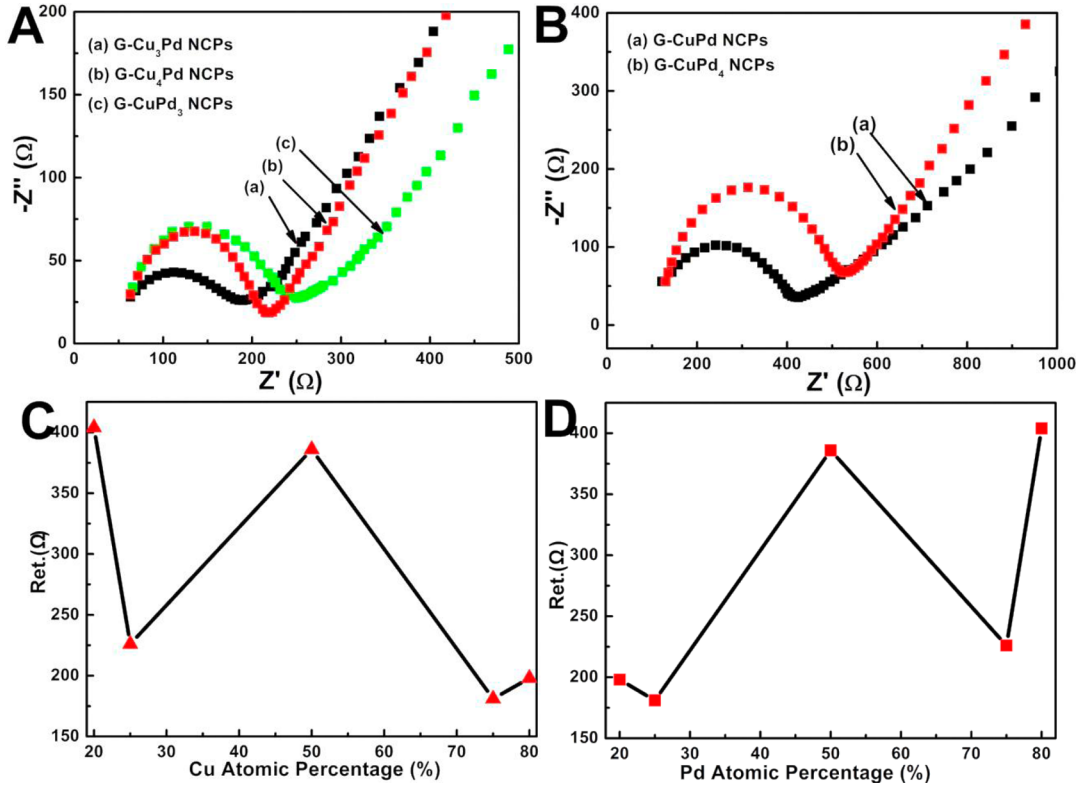

Figure 4. (A) Nyquist curves for G−Cu_3Pd (a), G−Cu_4Pd (b), and G−$CuPd_3$ (c) NCPs modified GCEs. (B) Nyquist curves for G−CuPd (a) and G−$CuPd_4$ (b) NCPs modified GCEs. (C, D) Plots of Ret values versus the atomic percentage of Cu (C) and Pd (D) in the Cu_xPd_y NCs components of the NCPs.

DOI: 10.1021/acsami.5b01541
ACS Appl. Mater. Interfaces 2015, 7, 5347−5357

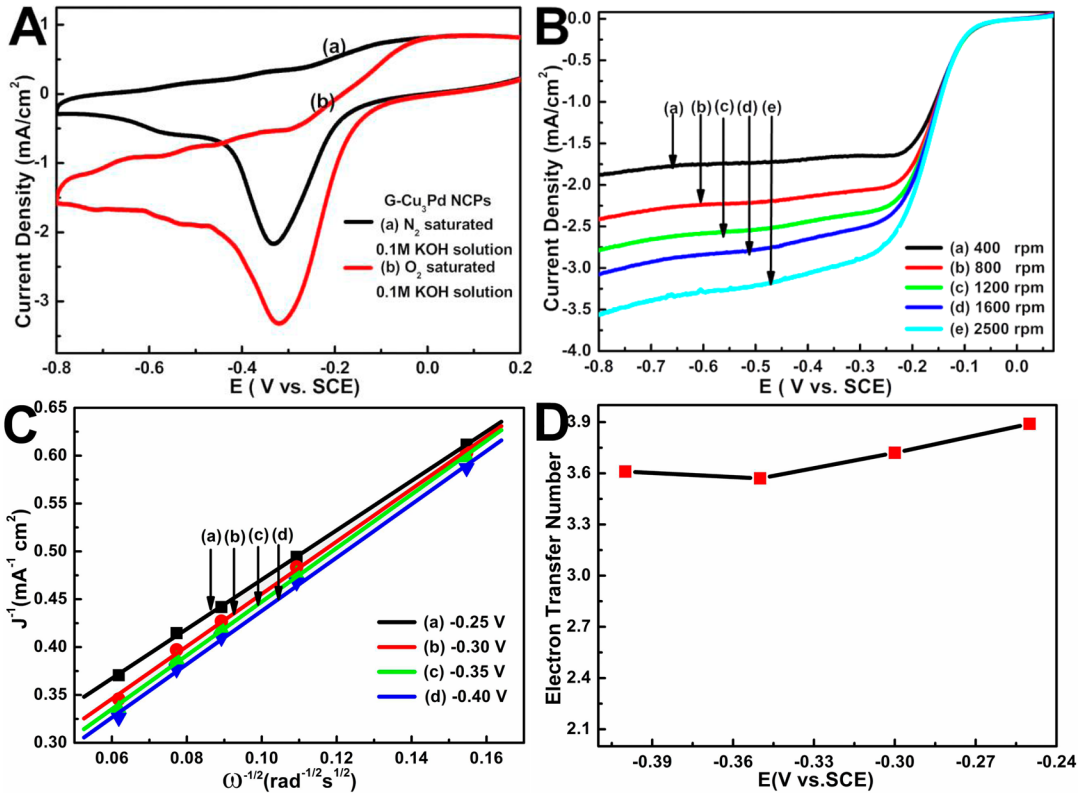

Figure 5. (A) Cyclic voltammetry plots of G−Cu_3Pd NCPs in (a) N_2- and (b) O_2-saturated 0.1 M KOH solution with a scan rate of 50 mV s^{-1}. (B) Rotating rate-dependent ORR polarization curves for G−Cu_3Pd NCPs with the scan rate of 10 mV s^{-1}. (C) Koutecky−Levich plots of J^{-1} vs $\omega^{-1/2}$ for G−Cu_3Pd NCPs at different potential obtained from B. (D) Plot of the number of transferred electrons versus potential for G−Cu_3Pd NCPs.

transfer resistance, which controls the electron transfer kinetics of the redox probe at the electrode interface; (3) W is the Warburg impedance that represents a kind of resistance to mass transfer; (4) CPE is the constant phase elements. The impedance of CPE can be expressed as the following equation: $(1/Z_{CPE}) = Y_{CPE} = Y_o(j\omega)^N$. Here, $\omega = 2\pi f$, Y_o represents the parameters of the whole circuit, and N stands for the smoothness degree of the electrode surface. For $N = 0$ and 1, the CPE represents the pure resistor and capacitor, respectively. The corresponding values of those four components are automatically given by the software in the Autolab electrochemical workstation after fitting the corresponding Nyquist curves. To observe clearly, parameters of the best-fitted results of EIS spectra for G−Cu_xPd_y NCPs and pure Cu_xPd_y NCs are summarized in Tables S2 and S3, Supporting Information, which are placed below Figures S9 and S10, Supporting Information, respectively. Compared with that of pure Cu_xPd_y NCs, the R_{et} values of the obtained five kinds of G−Cu_xPd_y NCPs are greatly decreased (Table S4, Supporting Information), implying that the presence of G can actually improve the interfacial electron transfer dynamics and facilitate electrocatalytic application. Among those G−Cu_xPd_y NCPs, the R_{et} value of G−Cu_3Pd NCPs (181 Ω) is much lower than that of G−Cu_4Pd (198 Ω), G−CuPd (386 Ω), G−$CuPd_3$ (226 Ω), and G−$CuPd_4$ (404 Ω), indicating a good conducting effect of G−Cu_3Pd NCPs in decreasing interfacial resistance and facilitating the electron transfer process at the electrode interface. Moreover, a relationship between the R_{et} values and Cu or Pd molar percentage can be found in the obtained G−Cu_xPd_y NCPs. With the increase of Cu atomic or molar percentage of Cu_xPd_y NCs components from 20% to 50% (Figure 4C), the R_{et} values of the NCPs first decrease and then increase. When increasing Cu molar percentage from 50% to 75%, the R_{et} values of the NCPs dramatically decrease and reach a minimal value at 75%. Further increasing the Cu molar percentage, the R_{et} value of the NCPs is slightly increased. This indicates that increasing the atomic percentage of Cu is helpful to reduce the R_{et} of the NCPs modified GCEs. On the contrary, the R_{et} value of the NCPs only decreases slightly as the molar percentage of Pd increase from 20% to 25% (Figure 4D). While increasing the molar percentage of Pd from 25% to 50%, the R_{et} values of the NCPs greatly increase, implying that improvement of Pd molar percentage in Cu_xPd_y NCs components leads to a much slower electron transfer process of the NCPs. Further increasing the Pd percentage from 50% to 80%, the R_{et} values of the NCPs slightly decrease and then dramatically increase at 80%. According to the literature,[47] metal Pd provides Ohmic contact that is beneficial to electron transfer at the solid interface. However, in our work, the Pd seems to exhibit a capacitive property, advantageous to store electrons. This abnormal phenomenon may be attributed to the presence of Cu that changes the electron transfer properties of Pd because the electronegativity of Cu (1.90) is slower than that of Pd (2.20). On the basis of our experiments, the observed differences of Cu and Pd molar percentage for the R_{et} of the NCPs may result from their different roles on the electron transfer process. To reduce the R_{et} and improve electrocatalytic performance of the NCPs, the G−Cu_3Pd NCPs modified GCE may be the optimal electrode for electrocatalytic reduction of oxygen. The subsequent electrocatalytic experiments give support for this viewpoint.

DOI: 10.1021/acsami.5b01541
ACS Appl. Mater. Interfaces 2015, 7, 5347−5357

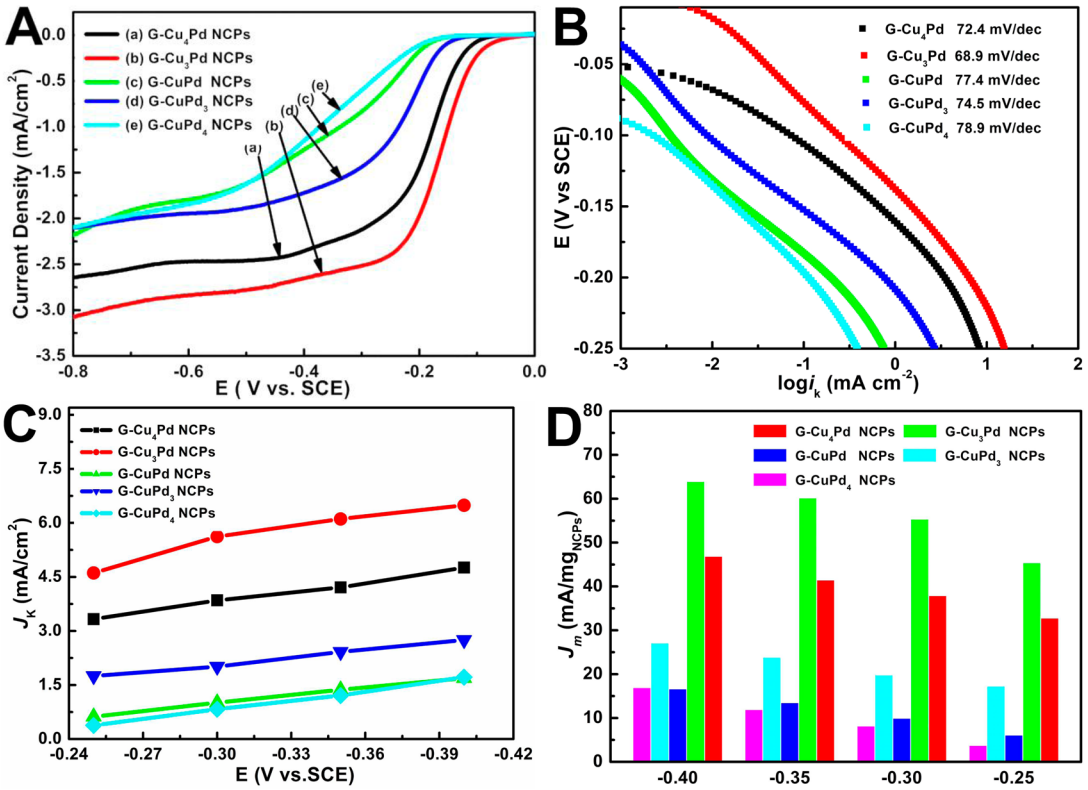

Figure 6. (A) ORR polarization curves of G−Cu_xPd_y NCPs at a rotating rate of 1600 rpm. (B) Tafel curves of G−Cu_xPd_y NCPs. (C) Kinetic current density (J_k) versus potential plots for G−Cu_xPd_y NCPs. (D) Mass activities of G−Cu_xPd_y NCPs under different potential. These values are calculated according to the loading mass of the NCPs.

The electrocatalytic performance of the obtained G−Cu_xPd_y NCPs was evaluated using ORR as a probe reaction. Figure 5A shows the cyclic voltammetry (CV) plots of the G−Cu_3Pd NCPs in N_2- and O_2-saturated 0.1 M KOH solution. An obvious and a strong reduction current peak is observed in O_2-saturated 0.1 M KOH solution compared with that in N_2-saturated the same electrolyte, indicating that G−Cu_3Pd NCPs possess a good electrocatalytic activity toward ORR. From the magnified CV plots at a potential from −0.3 to 0 V (Figure S11, Supporting Information), the onset oxygen reduction potential on G−Cu_3Pd NCPs is identified to be about −0.051 V vs SCE, which is much better than that of reported Ag-rich AgPd nanoalloy,[48] Cu nanowire−Ag NCs heterostructures,[49] Pt@Au−PyNG,[50] Cu_3N nanocubes,[51] G nanoplates[52] or quantum dots,[53] mesoporous Mn_2O_3-supported Pd NCs,[54] G−Ni-α-MnO_2 and −Cu-α-MnO_2 blends,[55] well-coupled G−$FePd_3$ NCPs,[56] and Pd/solid acid (HPW)/mesoporous carbon (CMK) three-component NCPs.[57] To get some insight on the catalytic behavior, the ORR at G−Cu_3Pd NCPs is further investigated by rotating disk voltammetry (RDV). Related ORR polarization curves at a rotating rate of 400, 800, 1200, 1600, and 2500 rpm are shown in Figure 5B. On the basis of those polarization curves, the number of transferred electrons (n) involved in the ORR process can be calculated according to the following Koutecky−Levich (K−L) equation[58]

$$\frac{1}{J} = \frac{1}{J_k} + \frac{1}{B\omega^{0.5}} \quad (1)$$

$$B = 0.62nF(D_{O2})^{2/3}\nu^{-1/6}C_{O2} \quad (2)$$

where J is the current density, J_k is the kinetic current density, ω is the rotating rate of the electrode, and B could be obtained from the Koutecky−Levich plots using eq 1. In addition, F in eq 2 is the Faraday constant (96 485 C mol^{-1}), D_{O_2} is the diffusion coefficient of O_2 in 0.1 M KOH (1.9×10^{-5} cm^2 s^{-1}), ν is the kinetic viscosity (0.01 cm^2 s^{-1}), C_{O_2} is the bulk concentration of O_2 (1.2×10^{-6} mol cm^{-3}), and the value of n represents the number of transferred electrons in the ORR process. The K−L plots of J^{-1} vs $\omega^{-1/2}$ at a potential of −0.25, −0.30, −0.35, and −0.40 V display good linearity (Figure 5C), indicating that the ORR on G−Cu_3Pd NCPs follows first-order kinetics. From the slope values ($1/B$) of the K−L plots, the n values for G−Cu_3Pd NCPs at −0.25, −0.30, −0.35, and −0.40 V can be calculated. Figure 5D gives the corresponding n value versus potential plot. It can be seen that the n values from −0.25 to −0.40 V are very close to 4.0, implying that the ORR mechanism on G−Cu_3Pd NCPs abides by the direct "4e$^-$" pathway ($O_2 + 2H_2O + 4e^- = 4OH^-$).

To understand the component effect of the obtained NCPs, the electrocatalytic properties of other G−Cu_xPd_y NCPs are also studied by RDV at a rotating rate of 1600 rpm. Corresponding ORR polarization plots for G−Cu_4Pd, G−CuPd, G−$CuPd_3$, and G−$CuPd_4$ NCPs are shown in Figure 6A. For comparison, the ORR polarization plot for G−Cu_3Pd NCPs at 1600 rpm is also given. Both their onset oxygen reduction potentials and apparent current density values follow the order G−Cu_3Pd > G−Cu_4Pd > G−$CuPd_3$ > G−CuPd > G−$CuPd_4$ NCPs. To further compare their catalytic activities, the corresponding Tafel plots for them are provided in Figure 6B. As is well known, the larger the Tafel slope, the lower the catalytic activity. The calculated Tafel slopes for G−Cu_4Pd, G−

DOI: 10.1021/acsami.5b01541
ACS Appl. Mater. Interfaces 2015, 7, 5347−5357

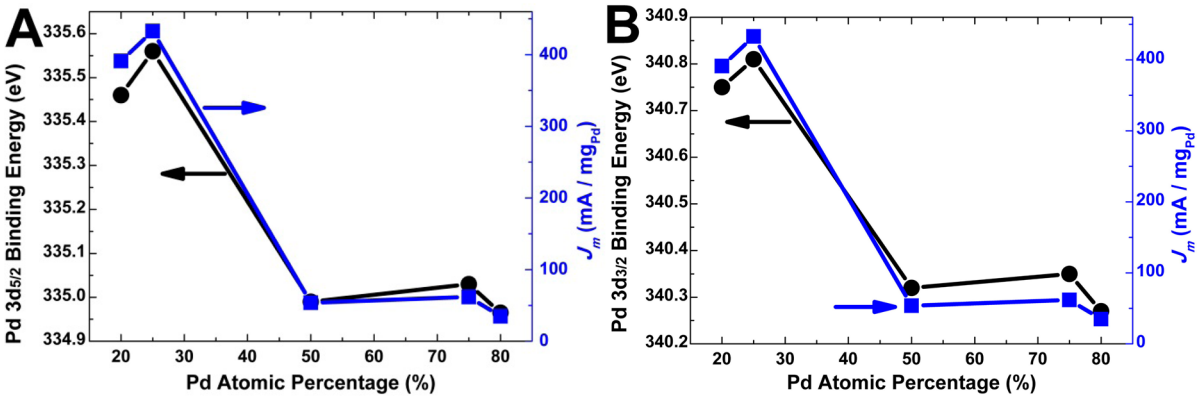

Figure 7. (A) Plots of the binding energies of Pd 3d5/2 for Cu_xPd_y NCs components and the mass specific activities of G−Cu_xPd_y NCPs at −0.40 V (vs SCE) versus the atomic percentage of Pd in Cu_xPd_y NCs components. (B) Plots of the binding energies of Pd 3d3/2 for Cu_xPd_y NCs components and the mass specific activities of G−Cu_xPd_y NCPs at −0.40 V (vs SCE) versus the atomic percentage of Pd in Cu_xPd_y NCs components.

$CuPd_3$, G−CuPd, and G−$CuPd_4$ NCPs are 72.4, 74.5, 77.4, and 78.9 mV/dec, respectively, which are much larger than G−Cu_3Pd NCPs (68.9 mV/dec), that is, the catalytic activity of G−Cu_4Pd, G−$CuPd_3$, G−CuPd, and G−$CuPd_4$ NCPs is lower than that of G−Cu_3Pd. Further evidence comes from the related kinetic current density (J_k) versus potential plots. As illustrated in Figure 6C, the J_k value of G−Cu_3Pd NCPs can reach 6.5 mA cm^{-2} at −0.40 V, which is nearly two times that of G−Cu_4Pd NCPs, four times that of G−$CuPd_3$ NCPs, and eight times that of G−CuPd and G−$CuPd_4$ NCPs. From the J_k versus potential plots, the mass specific activities (J_m) of those NCPs at different potential (Figure 6D) are further calculated according to the equation J_m = [J_k (kinetic current) × R_f (roughness factor)]/$L_{catalyst}$ (loading amount of the catalyst),[59] by assuming that the R_f value is approximately 1.0. At −0.25, −0.30, −0.35, and −0.40 V, the J_m values of the G−Cu_3Pd NCPs are 45.4, 55.3, 60.2, and 63.9 mA/mg_{NCPs}, respectively, which are much higher than G−Cu_4Pd, G−$CuPd_3$, G−CuPd, and G−$CuPd_4$ NCPs. It should be mentioned that the J_m values of G−Cu_3Pd NCPs at different potential will exceed 100 mA/mg_{Pd} if the mass of pure Pd in the NCPs is used to calculate the mass specific activity. For example, at −0.40 V, the J_m value of G−Cu_3Pd NCPs reaches 430 mA/mg_{Pd} (Figure S12, Supporting Information). All results reveal that G−Cu_3Pd NCPs possess the highest electrocatalytic activity.

To gain some insight on the best catalytic activity of G−Cu_3Pd NCPs among those G−Cu_xPd_y ones, we further analyze the XPS data of various Cu_xPd_y NCs components and correlate the binding energies of the Pd 3d peaks as well as the mass specific activities of the NCPs at −0.40 V with the Pd contents in the alloy NCs, as shown in Figure 7. The core-level binding energies of Pd 3d5/2 and Pd 3d3/2 peaks do not exhibit the monotonous change and show the complex double-volcano features toward high binding energy direction with the decrease of Pd or increase of Cu content. This suggests that the electronic coupling between Cu and Pd is very complicated, and the electronic structures of the alloy components are modulated by alloying of Pd with Cu. It is reported that the changes in the d-band center accompany the similar variations in the surface core-level shifts in the same direction.[60] Thus, the double-volcano type shifts in the binding energies of Pd 3d5/2 and Pd $3d_{3/2}$ peaks reflect the similar tendency of the d-band centers of those Cu_xPd_y NCs components relative to Fermi level. According to the Hammer-Nørskov model, there is a close correlation between the d-band center of a metal surface and its ability to form chemisorption bonds.[61] When the d-band center shifts up, the chemisorption bond will be significantly enhanced, which will improve the adsorption strength of active O_2 molecules and facilitate to break the O−O bond. On the contrary, as the d-band center shifts down, the chemisorption bond will obviously weaken which will decrease the chemical adsorption strength of reaction intermediates such as OH_{ads} in alkaline solution and lead to release of more electrochemically active sites available for ORR. Hence, regarding the counter balance between those two opposite effects related to the adsorption strength of active O_2 molecules and intermediates (OH_{ads}), there should be an optimum Pd 3d binding energy corresponding to the best catalytic activity for ORR on Cu_xPd_y alloy NCs with appropriate composition. In our work, the analogous double-volcano features are observed for the binding energies of Pd 3d peaks and the mass specific activities of G−Cu_xPd_y NCPs with the increase of Cu contents in Cu_xPd_y alloy components. These results indicate that the changes in the Pd core-level binding energy indeed affect the electrocatalytic ORR activity. Among the Cu_xPd_y NCs components, Cu_3Pd, which has the highest ORR activity, also has the highest value of the Pd 3d5/2 binding energy; this value is even higher than that of pure Pd NCs (335.2 eV). Except for Pd 3d5/2 peaks, the Pd 3d3/2 peaks also exhibit similar double-volcano tendencies and match the ORR activities well. Therefore, we conclude that the best electrocatalytic activity of G−Cu_3Pd NCPs compared with other G−Cu_xPd_y NCPs results primarily from their unique electronic structure or surface charge distribution, which probably facilitates activating O_2 molecules on Pd atomic sites and competitively adsorbing reaction intermediates on Cu atomic sites, that is, the ORR reaction on G−Cu_3Pd NCPs may be the synergistic catalytic effect between Cu and Pd and the metal elements play different roles on the catalytic reaction. Except for the component effect that caused the variations of electronic structure of alloy components, the size effect of Cu_xPd_y NCs in those G−Cu_xPd_y NCPs may be another possible reason that the G−Cu_3Pd NCPs exhibit the highest electrocatalytic activity. Usually, the smaller the size, the higher the catalytic activity. Figure S13, Supporting Information, gives the plots for the size of Cu_xPd_y NCs and mass specific activities of G−Cu_xPd_y NCPs at −0.40 V versus the atomic percentage of Pd in Cu_xPd_y NCs, from which we can see that the size of

DOI: 10.1021/acsami.5b01541
ACS Appl. Mater. Interfaces 2015, 7, 5347−5357

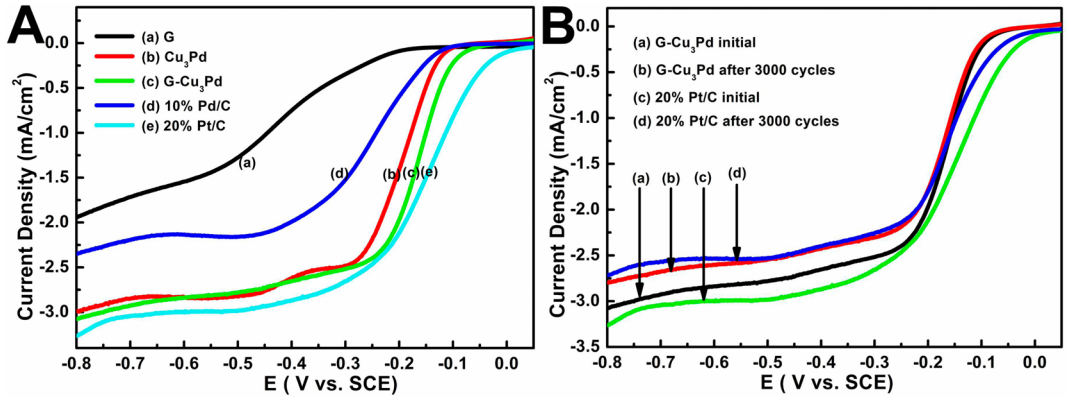

Figure 8. (A) ORR polarization curves for pure G, pure Cu_3Pd NCs, G−Cu_3Pd NCPs, commercial Pd/C, and Pt/C catalysts. (B) Durability tests for G−Cu_3Pd NCPs and commercial Pt/C catalyst. The rotation rate of the glassy carbon disk electrode is 1600 rpm.

Cu_3Pd NCs is the smallest among all the G−Cu_xPd_y NCPs. Thus, the G−Cu_3Pd NCPs possess the highest catalytic activity.

Moreover, to get further insight on the origin of the excellent electrocatalytic activity observed in G−Cu_3Pd NCPs, the electrocatalytic properties of pure G and Cu_3Pd NCs as well as commercial Pd/C and Pt/C catalysts are also studied by RDV under the same experimental conditions. Related ORR polarization plots are shown in Figure 8A, from which we can see that the onset reduction potential of G−Cu_3Pd NCPs is more positive than pure G and Cu_3Pd NCs. Additionally, in contrast to pure G and Cu_3Pd NCs, the apparent current density of G−Cu_3Pd NCPs is also greatly enhanced, that is, the electrocatalytic activity of G−Cu_3Pd NCPs is higher than that of pure G and Cu_3Pd NCs. The size and shape of Cu_3Pd NCs components in G−Cu_3Pd NCPs are identical to that of pure Cu_3Pd NCs, so the enhanced catalytic activity observed in G−Cu_3Pd NCPs originates from the presence of G and a strong synergetic effect between Cu_3Pd NCs and G that leads to enhanced interfacial electron transfer dynamics, as evidenced by EIS spectra. In addition, the electrocatalytic activity of G−Cu_3Pd NCPs is also better than commercial Pd/C (10%) and close to Pt/C (20%) catalysts, indicating that G−Cu_3Pd NCPs are actually a promising ORR electrocatalyst for application in alkaline fuel cells with the advantage of high activity and low cost.

Except for the catalytic activity, the stability or long durability is another important parameter for determining the practical application of a special electrocatalyst.[62] The durability tests for G−Cu_3Pd NCPs and commercial Pt/C (20%) catalyst are further performed, shown in Figure 8B. As for G−Cu_3Pd NCPs, after continuous cycling 3000 times in O_2-saturated 0.1 M KOH solution, their onset reduction potential is nearly unchanged and 91.2% of initial current density can be reserved. By magnifying the ORR polarization plots before and after the cycling test (Figure S14, Supporting Information), we can find that the semiwave potential of G−Cu_3Pd NCPs only decreases 7.1 mV, while for commercial Pt/C (20%) catalyst its onset potential becomes more negative and only 84.4% of initial current density can be retained after continuous 3000 cycles in O_2-saturated 0.1 M KOH solution. Also, its semiwave potential decreases 17.2 mV, which is much larger than that of G−Cu_3Pd NCPs. A similar phenomenon has been observed by Sun and coauthors in their recent work on Ag/Au@CuPd core−shell catalyst.[63] These results demonstrate that the stability or long durability of G−Cu_3Pd NCPs is much better than that of commercial Pt/C catalyst, albeit the catalytic activity of the former is slightly lower than that of the latter. Further work on the synergistic strain and electronic and geometric effects to improve the performance of Cu-enriched alloy catalyst for ORR is underway in our lab.

4. CONCLUSIONS

In summary, a series of G−Cu_xPd_y (Cu_4Pd, Cu_3Pd, CuPd, $CuPd_3$, and $CuPd_4$) NCPs has been synthesized by integrating or assembling presynthesized monodisperse Cu_xPd_y NCs on G sheets. In those NCPs, the Cu_xPd_y NCs are fcc structure with high crystallinity, which are well dispersed on the planar plane, crumples, or edges of the G and show component-dependent electronic structure. Compared with pure Cu_xPd_y NCs, the greatly enhanced interfacial electron transfer dynamics are observed in those G−Cu_xPd_y NCPs, which exhibit a strong correlation with the alloy compositions of the NCPs. Related electrocatalytic tests in alkaline media reveal that the ORR activities of those G−Cu_xPd_y NCPs are also strongly dependent on alloy components. Also, there is a double-volcano-type correlation between the ORR activities and the alloy compositions of those NCPs. Among them, G−Cu_3Pd NCPs exhibit the highest electrocatalytic activity compared with other G−Cu_xPd_y ones, which is much better than that of some reported materials (e.g., Pd−Ag alloy, Pt@Au−PyNG, Pd/HPW/CMK NCPs) and commercial Pd/C catalyst and close to Pt/C catalyst. By correlating the Pd 3d binding energies and the sizes of Cu_xPd_y NCs with the mass specific activities of G−Cu_xPd_y NCPs and considering the interfacial electron transfer dynamics, the best catalytic activity of G−Cu_3Pd NCPs may be attributed to the unique electronic structure and the smallest size of Cu_3Pd NCs as well as the strong synergistic effect between G and Cu_3Pd NCs. Most importantly, the durability of G−Cu_3Pd NCPs is superior to commercial Pt/C catalyst, implying that G−Cu_3Pd NCPs are an alternative electrocatalyst for Pt/C to use in alkaline fuel cells. This work not only realizes the component-controlled synthesis and assembly of Cu_xPd_y NCs on G to obtain advanced NCPs but also screens out a low-cost Cu-rich hybrid electrocatalyst for ORR with high activity and stability. Also, it paves the way for in the future developing cost-effective Cu-rich nanoalloy catalyst to apply in other technological fields, such as metal−air batteries, CO_2 conversion and utilization, and biosensing fields.

DOI: 10.1021/acsami.5b01541
ACS Appl. Mater. Interfaces 2015, 7, 5347−5357

■ ASSOCIATED CONTENT

Supporting Information

Composition characterization of presynthesized Cu_xPd_y NCs, TEM images of pure Cu and pure Pd control samples, surface electronic structure analysis of Cu_xPd_y NCs, additional component characterization of G−Cu_xPd_y NCPs, EIS data for Cu_xPd_y NCs, equivalent circuits for fitting the Nyquist curves of G−Cu_xPd_y NCPs and pure Cu_xPd_y NCs, parameters of the best-fitted results of EIS spectra as well as a comparison of their R_{et} values, and additional electrochemical data for G−Cu_3Pd NCPs. This material is available free of charge via the Internet at http://pubs.acs.org.

■ AUTHOR INFORMATION

Corresponding Authors

* Phone: +86-25-85891051. Fax: +86-25-85891051. E-mail: 07203@njnu.edu.cn.

* Phone: +86-25-85891051. Fax: +86-25-85891051. E-mail: daizhihuii@njnu.edu.cn.

Notes

The authors declare no competing financial interest.

■ ACKNOWLEDGMENTS

This work was supported by the National Natural Science Foundation of China (Nos. 21271105, 21175069, and 21171096), research fund from the Priority Academic Program Development of Jiangsu Higher Education Institutions, and the opening research foundations of State Key Laboratory of Coordination Chemistry, Nanjing National Laboratory of Solid State Microstructures, Nanjing University.

■ REFERENCES

(1) Novoselov, K. S.; Fal'ko, V. I.; Colombo, L.; Gellert, P. R.; Schwab, M. G.; Kim, K. A Roadmap for Graphene. *Nature* **2012**, *490*, 192−200.

(2) Xin, S.; Guo, Y. G.; Wan, L. J. Nanocarbon Networks for Advanced Rechargeable Lithium Batteries. *Acc. Chem. Res.* **2012**, *45*, 1759−1769.

(3) Dai, L. M. Functionalization of Graphene for Efficient Energy Conversion and Storage. *Acc. Chem. Res.* **2013**, *46*, 31−42.

(4) Tan, C. L.; Huang, X.; Zhang, H. Synthesis and Application of Graphene-Based Noble Metal Nanostructures. *Mater. Today* **2013**, *16*, 29−36.

(5) Hu, S.; Lozada-Hidalgo, M.; Wang, F. C.; Mishchenko, A.; Schedin, F.; Nair, R. R.; Hill, E. W.; Boukhvalov, D. W.; Katsnelson, M. I.; Dryfe, R. A. W.; Grigorieva, I. V.; Wu, H. A.; Geim, A. K. Proton Transport Through One-Atom-Thick Crystals. *Nature* **2014**, *516*, 227−230.

(6) Primo, A.; Neatu, F.; Florea, M.; Parvulescu, V.; Garcia, H. Graphenes in the Absence of Metals as Carbocatalysts for Selective Acetylene Hydrogenation and Alkene Hydrogenation. *Nat. Commun.* **2014**, *5*, 5291.

(7) Yang, M.-Q.; Zhang, N.; Pagliaro, M.; Xu, Y.-J. Artificial Photosynthesis over Graphene-Semiconductor Composites. Are We Getting Better? *Chem. Soc. Rev.* **2014**, *43*, 8240−8254.

(8) Liu, M. M.; Lu, Y. Z.; Chen, W. PdAg Nanorings Supported on Graphene Nanosheets: Highly Methanol-Tolerant Cathode Electrocatalyst for Alkaline Fuel Cells. *Adv. Funct. Mater.* **2013**, *23*, 1289−1296.

(9) Wang, H. L.; Dai, H. J. Strongly Coupled Inorganic-Nano-Carbon Hybrid Materials for Energy Storage. *Chem. Soc. Rev.* **2013**, *42*, 3088−3113.

(10) Kou, R.; Shao, Y. Y.; Mei, D. H.; Nie, Z. M.; Wang, D. H.; Wang, C. M.; Viswanathan, V. V.; Park, S.; Aksay, I. A.; Lin, Y. H.; Wang, Y.; Liu, J. Stabilization of Electrocatalytic Metal Nanoparticles at Metal-Metal Oxide-Graphene Triple Junction Points. *J. Am. Chem. Soc.* **2011**, *133*, 2541−2547.

(11) Guo, S. J.; Dong, S. J.; Wang, E. K. Three-Dimensional Pt-on-Pd Bimetallic Nanodendrites Supported on Graphene Nanosheet: Facile Synthesis and Use as Advanced Nanoelectrocatalyst for Methanol Oxidation. *ACS Nano* **2010**, *4*, 547−555.

(12) Chen, X. M.; Wu, G. H.; Chen, J. M.; Chen, X.; Xie, Z. X.; Wang, X. R. Synthesis of "Clean" and Well-Dispersive Pd Nanoparticles with Excellent Electrocatalytic Property on Graphene Oxide. *J. Am. Chem. Soc.* **2011**, *133*, 3693−3695.

(13) Zhang, J.; Yu, J. G.; Jaroniec, M.; Gong, J. R. Noble-Metal Free Reduced Graphene Oxide-$Zn_xCd_{1-x}S$ Nanocomposite with Enhanced Solar Photocatalytic H_2 Production Performance. *Nano Lett.* **2012**, *12*, 4584−4589.

(14) Liang, Y. Y.; Li, Y. G.; Wang, H. L.; Zhou, J. G.; Wang, J.; Regier, T.; Dai, H. J. Co_3O_4 Nanocrystals on Graphene as a Synergistic Catalyst for Oxygen Reduction Reaction. *Nat. Mater.* **2011**, *10*, 780−786.

(15) Wang, H. L.; Liang, Y. Y.; Li, Y. G.; Dai, H. J. $Co_{1-x}S$-Graphene Hybrid: A High-Performance Metal Chalcogenide Electrocatalyst for Oxygen Reduction. *Angew. Chem., Int. Ed.* **2011**, *50*, 10969−10972.

(16) Tang, H.; Yin, H.; Wang, J.; Yang, N.; Wang, D.; Tang, Z. Molecular Architecture of Cobalt Porphyrin Multilayers on Reduced Graphene Oxide Sheets for High-Performance Oxygen Reduction Reaction. *Angew. Chem., Int. Ed.* **2013**, *52*, 5585−5589.

(17) Guo, S. J.; Sun, S. H. FePt Nanoparticles Assembled on Graphene as Enhanced Catalyst for Oxygen Reduction Reaction. *J. Am. Chem. Soc.* **2012**, *134*, 2492−2495.

(18) Lu, L.; Chen, X.; Huang, X.; Lu, K. Revealing the Maximum Strength in Nanotwinned Copper. *Science* **2009**, *323*, 607−610.

(19) Ye, S. R.; Rathmell, A. R.; Chen, Z. F.; Stewart, I. E.; Wiley, B. J. Metal Nanowire Networks: The Next Generation of Transparent Conductors. *Adv. Mater.* **2014**, *26*, 6670−6687.

(20) He, R.; Wang, Y.-C.; Wang, X.; Wang, Z.; Liu, G.; Zhou, W.; Wen, L.; Li, Q.; Wang, X.; Chen, X.; Zeng, J.; Hou, J. G. Facile Synthesis of Pentacle Gold-Copper Alloy Nanocrystals and Their Plasmonic and Catalytic Properties. *Nat. Commun.* **2014**, *5*, 4327.

(21) Kim, D.; Resasco, J.; Yu, Y.; Asiri, A. M.; Yang, P. D. Synergistic Geometric and Electronic Effects for Electrochemical Reduction of Carbon Dioxide Using Gold-Copper Bimetallic Nanoparticles. *Nat. Commun.* **2014**, *5*, 4948.

(22) Li, C. W.; Ciston, J.; Kanan, M. W. Electroreduction of Carbon Monoxide to Liquid Fuel on Oxide-Derived Nanocrystalline Copper. *Nature* **2014**, *508*, 504−507.

(23) Sen, S.; Liu, D.; Palmore, G. T. R. Electrochemical Reduction of CO_2 at Copper Nanofoams. *ACS Catal.* **2014**, *4*, 3091−3095.

(24) Wu, Z. N.; Li, Y. C.; Liu, J. L.; Lu, Z. Y.; Zhang, H.; Yang, B. Colloidal Self-Assembly of Catalytic Copper Nanoclusters into Ultrathin Ribbons. *Angew. Chem., Int. Ed.* **2014**, *53*, 12196−12200.

(25) Wang, J.; Wang, K.; Wang, F.-B.; Xia, X.-H. Bioinspired Copper Catalyst Effective for Both Reduction and Evolution of Oxygen. *Nat. Commun.* **2014**, *5*, 5285.

(26) Wang, D. L.; Yu, Y. C.; Xin, H. L. L.; Hovden, R.; Ercius, P.; Mundy, J. A.; Chen, H.; Richard, J. H.; Muller, D. A.; DiSalvo, F. J.; Abruña, H. D. Tuning Oxygen Reduction Reaction Activity via Controllable Dealloying: A Model Study of Ordered Cu_3Pt/C Intermetallic Nanocatalysts. *Nano Lett.* **2012**, *12*, 5230−5238.

(27) Wang, G. W.; Xiao, L.; Huang, B.; Ren, Z. D.; Tang, X.; Zhuang, L.; Lu, J. T. AuCu Intermetallic Nanoparticles: Surfactant-Free Synthesis and Novel Electrochemistry. *J. Mater. Chem.* **2012**, *22*, 15769−15774.

(28) Wang, X. P.; Kariuki, N. N.; Vaughey, J. T.; Goodpaster, J.; Kumar, R.; Myers, D. J. Bimetallic Pd-Cu Oxygen Reduction Electrocatalysts. *J. Electrochem. Soc.* **2008**, *155*, B602−B609.

(29) Kariuki, N. N.; Wang, X. P.; Mawdsley, J. R.; Ferrandon, M. S.; Niyogi, S. G.; Vaughey, J. T.; Myers, D. J. Colloidal Synthesis and Characterization of Carbon-Supported Pd-Cu Nanoparticle Oxygen Reduction Electrocatalysts. *Chem. Mater.* **2010**, *22*, 4144−4152.

DOI: 10.1021/acsami.5b01541
ACS Appl. Mater. Interfaces 2015, 7, 5347−5357

(30) Mazumder, V.; Chi, M. F.; Mankin, M. N.; Liu, Y.; Metin, O.; Sun, D. H.; More, K. L.; Sun, S. H. A Facile Synthesis of MPd (M = Co, Cu) Nanoparticles and Their Catalysis for Formic Acid Oxidation. *Nano Lett.* **2012**, *12*, 1102−1106.
(31) Yamauchi, M.; Abe, R.; Tsukuda, T.; Kato, K.; Takata, M. Highly Selective Ammonia Synthesis from Nitrate with Photocatalytically Generated Hydrogen on CuPd/TiO_2. *J. Am. Chem. Soc.* **2011**, *133*, 1150−1152.
(32) Xi, P. X.; Cao, Y.; Yang, F. C.; Ma, C.; Chen, F. J.; Yu, S.; Wang, S.; Zeng, Z. Z.; Zhang, X. Facile Synthesis of Pd-Based Bimetallic Nanocrystals and Their Application as Catalysts for Methanol Oxidation Reaction. *Nanoscale* **2013**, *5*, 6124−6130.
(33) Ho, S. F.; Mendoza-Garcia, A.; Guo, S. J.; He, K.; Su, D.; Liu, S.; Metin, O.; Sun, S. H. A Facile Route to Monodisperse MPd (M = Co or Cu) Alloy Nanoparticles and Their Catalysis for Electrooxidation of Formic Acid. *Nanoscale* **2014**, *6*, 6970−6973.
(34) Zhang, L.; Hou, F.; Tan, Y. W. Shape-Tailoring of CuPd Nanocrystals for Enhancement of Electro-catalytic Activity in Oxygen Reduction Reaction. *Chem. Commun.* **2012**, *48*, 7152−7154.
(35) Xu, C. X.; Liu, Y. Q.; Wang, J. P.; Geng, H. R.; Qiu, H. J. Fabrication of Nanoporous Cu-Pt(Pd) Core/Shell Structure by Galvanic Replacement and its Application in Electrocatalysis. *ACS Appl. Mater. Interfaces* **2011**, *3*, 4626−4632.
(36) Hu, C. G.; Guo, Y. M.; Wang, J. L.; Yang, L.; Yang, Z. X.; Bai, Z. Y.; Zhang, J.; Wang, K.; Jiang, K. Additive-Free Fabrication of Spherical Hollow Palladium/Copper Alloyed Nano- structures for Fuel Cell Application. *ACS Appl. Mater. Interfaces* **2012**, *4*, 4461−4464.
(37) Chen, S. T.; Jenkins, S. V.; Tao, J.; Zhu, Y. M.; Chen, J. Y. Anisotropic Seeded Growth of Cu-M (M = Au, Pt, or Pd) Bimetallic Nanorods with Tunable Optical and Catalytic Properties. *J. Phys. Chem. C* **2013**, *117*, 8924−8932.
(38) Mohl, M.; Dobo, D.; Kukovecz, A.; Konya, Z.; Kordas, K.; Wei, J. Q.; Vajtai, R.; Ajayan, P. M. Formation of CuPd and CuPt Bimetallic Nanotubes by Galvanic Replacement Reaction. *J. Phys. Chem. C* **2011**, *115*, 9403−9409.
(39) Xu, C. X.; Zhang, Y.; Wang, L. Q.; Xu, L. Q.; Bian, X. F.; Ma, H. Y.; Ding, Y. Nanotubular Mesoporous PdCu Bimetallic Electrocatalysts toward Oxygen Reduction Reaction. *Chem. Mater.* **2009**, *21*, 3110−3116.
(40) Shao, M. H.; Shoemaker, K.; Peles, A.; Kaneko, K.; Protsailo, L. Pt Monolayer on Porous Pd-Cu Alloys as Oxygen Reduction Electrocatalysts. *J. Am. Chem. Soc.* **2010**, *132*, 9253−9255.
(41) Zhang, Y. W.; Huang, W. Y.; Habas, S. E.; Kuhn, J. N.; Grass, M. E.; Yamada, Y.; Yang, P. D.; Somorjai, G. A. Near-Monodisperse Ni-Cu Bimetallic Nanocrystals of Variable Composition: Controlled Synthesis and Catalytic Activity for H_2 Generation. *J. Phys. Chem. C* **2008**, *112*, 12092−12095.
(42) Xu, D.; Bliznakov, S.; Liu, Z. P.; Fang, J. Y.; Dimitrov, N. Composition-Dependent Electrocatalytic Activity of Pt-Cu Nanocube Catalysts for Formic Acid Oxidation. *Angew. Chem., Int. Ed.* **2010**, *49*, 1282−1285.
(43) Hummers, W. S.; Offeman, R. E. Preparation of Graphitic Oxide. *J. Am. Chem. Soc.* **1958**, *80*, 1339−1339.
(44) Ferrari, A. C.; Basko, D. M. Raman Spectroscopy as a Versatile Tool for Studying the Properties of Graphene. *Nat. Nanotechnol.* **2013**, *8*, 235−246.
(45) Gao, L. B.; Ren, W. C.; Liu, B. L.; Saito, R.; Wu, Z. S.; Li, S. S.; Jiang, C. B.; Li, F.; Cheng, H. M. Surface and Interference Coenhanced Raman Scattering of Graphene. *ACS Nano* **2009**, *3*, 933−939.
(46) Giovanni, M.; Poh, H. L.; Ambrosi, A.; Zhao, G. J.; Khezri, B.; Webster, R. D.; Pumera, M. Noble Metal (Pd, Ru, Rh, Pt, Au, Ag) Doped Graphene Hybrids for Electrocatalysis. *Nanoscale* **2012**, *4*, 5002−5008.
(47) Takai, A.; Kamat, P. V. Capture, Storage, and Discharge. Shuttling Photogenerated Electrons across TiO_2-Ag Interface. *ACS Nano* **2011**, *5*, 7369−7376.
(48) Slanac, D. A.; Hardin, W. G.; Johnston, K. P.; Stevenson, K. J. Atomic Ensemble and Electronic Effects in Ag-Rich AgPd Nanoalloy Catalysts for Oxygen Reduction in Alkaline Media. *J. Am. Chem. Soc.* **2012**, *134*, 9812−9819.
(49) Han, M.; Liu, S. L.; Zhang, L. Y.; Zhang, C.; Tu, W. W.; Dai, Z. H.; Bao, J. C. Synthesis of Octopus-Tentacle-Like Cu Nanowire-Ag Nanocrystals Heterostructures and Their Enhanced Electrocatalytic Performance for Oxygen Reduction Reaction. *ACS Appl. Mater. Interfaces* **2012**, *4*, 6654−6650.
(50) Zhong, X.; Yu, H. Y.; Wang, X. D.; Liu, L.; Jiang, Y.; Wang, L.; Zhuang, G. L.; Chu, Y. Q.; Li, X. N.; Wang, J.-Q. Pt@Au Nanorods Uniformly Decorated on Pyridyne Cycloaddition Graphene as a Highly Effective Electrocatalyst for Oxygen Reduction. *ACS Appl. Mater. Interfaces* **2014**, *6*, 13448−13454.
(51) Wu, H. B.; Chen, W. Copper Nitride Nanocubes: Size-Controlled Synthesis and Application as Cathode Catalyst in Alkaline Fuel Cells. *J. Am. Chem. Soc.* **2011**, *133*, 15236−15239.
(52) Jeon, I. Y.; Choi, H. J.; Jung, S. M.; Seo, J. M.; Kim, M. J.; Dai, L. M.; Baek, J. B. Large-Scale Production of Edge-Selectively Functionalized Graphene Nanoplatelets via Ball Milling and Their Use as Metal-Free Electrocatalysts for Oxygen Reduction Reaction. *J. Am. Chem. Soc.* **2013**, *135*, 1386−1393.
(53) Li, Y.; Zhao, Y.; Cheng, H. H.; Hu, Y.; Shi, G. Q.; Dai, L. M.; Qu, L. T. Nitrogen-Doped Graphene Quantum Dots with Oxygen-Rich Functional Groups. *J. Am. Chem. Soc.* **2012**, *134*, 15−18.
(54) Dong, H.-Q.; Chen, Y.-Y.; Han, M.; Li, S.-L.; Zhang, J.; Li, J.-S.; Lan, Y.-Q.; Dai, Z. H.; Bao, J. C. Synergistic Effect of Mesoporous Mn_2O_3-Supported Pd Nanoparticle Catalysts for Electrocatalytic Oxygen Reduction Reaction with Enhanced Performance in Alkaline Medium. *J. Mater. Chem. A* **2014**, *2*, 1272−1276.
(55) Lambert, T. N.; Danae, J.; Lu, W.; Limmer, S. J.; Kotula, P. G.; Thuli, A.; Hungate, M.; Ruan, G. D.; Jin, Z.; Tour, J. M. Graphene-Ni-alpha-MnO_2 and -Cu-alpha-MnO_2 Nanowire Blends as Highly Active Non-precious Metal Catalysts for the Oxygen Reduction Reaction. *Chem. Commun.* **2012**, *48*, 7931−7933.
(56) Yin, H. H.; Liu, S. L.; Zhang, C. L.; Bao, J. C.; Zheng, Y. L.; Han, M.; Dai, Z. H. Well-Coupled Graphene and Pd-Based Bimetallic Nanocrystals Nanocomposites for Electrocatalytic Oxygen Reduction Reaction. *ACS Appl. Mater. Interfaces* **2014**, *6*, 2086−2094.
(57) Liu, H.; Zheng, Y.; Wang, G. X.; Qiao, S. Z. Three-Component Nanocomposite with Synergistic Reactivity for Oxygen Reduction Reaction in Alkaline Solution. *Adv. Energy Mater.* **2014**, DOI: 10.1002/aenm.201401186.
(58) Parvez, K.; Yang, S. B.; Hernandez, Y.; Winter, A.; Turchanin, A.; Feng, X. L.; Müllen, K. Nitrogen-Doped Graphene and Its Iron-Based Composite as Efficient Electrocatalysts for Oxygen Reduction Reaction. *ACS Nano* **2012**, *6*, 9541−9550.
(59) Mayrhofer, K. J. J.; Strmcnik, D.; Blizanac, B. B.; Stamenkovic, V.; Arenz, M.; Markovic, N. M. Measurement of Oxygen Reduction Activities via the Rotating Disc Electrode Method: From Pt Model Surfaces to Carbon-Supported High Surface Area Catalysts. *Electrochim. Acta* **2008**, *53*, 3181−3188.
(60) Zhao, Y. G.; Liu, J. J.; Zhao, Y. H.; Wang, F. Composition-Controlled Synthesis of Carbon-Supported Pt-Co Alloy Nanoparticles and the Origin of Their ORR Activity Enhancement. *Phys. Chem. Chem. Phys.* **2014**, *16*, 19298−19306.
(61) Hammer, B.; Nørskov, J. K. Theoretical Surface Science and Catalysis-Calculations and Concepts. *Adv. Catal.* **2000**, *45*, 71−129.
(62) Wang, C.; van der Vliet, D.; More, K. L.; Zaluzec, N. J.; Peng, S.; Sun, S. H.; Daimon, H.; Wang, G.; Greeley, J.; Pearson, J.; Paulikas, A. P.; Karapetrov, G.; Strmcnik, D.; Markovic, N. M.; Stamenkovic, V. R. Multimetallic Au/$FePt_3$ Nanoparticles as Highly Durable Electrocatalyst. *Nano Lett.* **2011**, *11*, 919−926.
(63) Guo, S. J.; Zhang, X.; Zhu, W. L.; He, K.; Su, D.; Mendoza-Garcia, A.; Ho, S. F.; Lu, G.; Sun, S. H. Nanocatalyst Superior to Pt for Oxygen Reduction Reaction: the Case of Core/Shell Ag (Au)/CuPd Nanoparticles. *J. Am. Chem. Soc.* **2014**, *136*, 15026−15033.

DOI: 10.1021/acsami.5b01541
ACS Appl. Mater. Interfaces 2015, 7, 5347−5357